Formation of Intermetallic Compounds in a Cold-Sprayed Aluminum Coating on Magnesium Alloy Substrate after Friction Stir-Spot-Processing

Gang Ji[1] · Hong Liu[1] · Guan-Jun Yang[1] · Xiao-Tao Luo[1] · Cheng-Xin Li[1] ·
Guang-yu He[2] · Li Zhou[3] · Tao Liang[3]

Abstract Magnesium-based alloys are appropriate materials for transportation applications owing to their high strength-to-weight ratio. However, the poor corrosion performance of Mg alloy limits its lifetime. In this study, the pure Al coating was deposited onto an AZ91D substrate by cold spraying, and then modified by friction stir-spot-processing. The interfacial microstructure and phase were studied in detail, and the effect of the intermetallic compounds on the microhardness and corrosion properties of the coatings was investigated. Results show that the sound and dense coatings were obtained after friction stir-spot-processing at 2400 and 2700 rpm. $Al_{12}Mg_{17}$ was found in the upper part of the 1/2 radius zone in the processed coating. The thin and thick IMCs were identified at the interface in the center and 1/2 radius areas, respectively. In the thick IMCs, mainly two types of multi-phase coexistence structures were observed. The four-phase coexistence structure dominated by Al_3Mg_2 revealed a higher microhardness than the three-phase coexistence structure dominated by $Al_{12}Mg_{17}$. In the processed coating, the upper part of the 1/2 radius zone containing $Al_{12}Mg_{17}$ exhibited a higher microhardness than the center zone. Moreover, the cold-sprayed Al coating provided more effective corrosion protection for the AZ91D substrate after FSSP.

Introduction

In the past years, magnesium (Mg)-based alloys have received increasing attention as structural components in the transportation industry due to their superior mechanical properties, high strength-to-weight ratio, and excellent damping resistance (Ref 1). AZ91D is one of the most prevalent commercial casting magnesium alloys which is widely used in cell phone and computer cases, aircraft control systems, and car steering wheel brackets (Ref 2). However, the inferior corrosion resistance of AZ91D limits its lifetime (Ref 3). Therefore, different protective coatings, such as Al coating and Al-enriched surface alloyed layer, are usually prepared to avoid the degradation of AZ91D (Ref 4-7).

Cold spraying is an advanced solid-state coating technology, which utilizes a supersonic jet to accelerate solid metallic particles toward a substrate (Ref 8-10). The high velocity, instead of elevated temperature, is utilized to develop the plastic deformation of the deposited particles and obtain the desired coating. The oxidation of the particles will be avoided during spraying (Ref 11, 12). However, one should note that the cold spraying usually produces interfacial bonds by the mechanical interlocking (Ref 13), resulting in low interfacial strength.

Friction stir processing (FSP), based on friction stir welding (FSW) (Ref 14-17), has been developed as a novel

✉ Hong Liu
   hongliu@mail.xjtu.edu.cn

1   State Key Laboratory for Mechanical Behavior of Materials,
    School of Materials Science and Engineering, Xi'an Jiaotong
    University, Xi'an 710049, Shaanxi, China

2   Science and Technology on Plasma Dynamics Laboratory,
    Air Force Engineering University, Xi'an 710038, Shaanxi,
    China

3   Shandong Provincial Key Laboratory of Special Welding
    Technology, Harbin Institute of Technology at Weihai,
    Weihai 264209, Shandong, China

solid-state treatment method (Ref 18). The friction heat and plastic deformation generated during FSSP enhance the microstructures and properties of the materials. Hence, FSP is a promising route to improve the microstructure, mechanical properties, and service performance of the cold-sprayed coatings (Ref 19, 20). Hodder et al. (Ref 21) carried out FSP on the cold-sprayed Al-Al$_2$O$_3$ coatings, in which the coating hardness was improved due to the redistribution and refinement of Al$_2$O$_3$ particles. Li et al. (Ref 22) modified the cold-sprayed Cu-Zn coating by FSP and found that the refined grains enhanced the mechanical properties. Khodabakhshi et al. (Ref 23) used FSP to modify the cold-sprayed Ti coating and studied the residual stress in the coating after FSP. Yang et al. (Ref 24) applied FSP to the cold-sprayed AA2024/Al$_2$O$_3$ coatings and reported an enhanced corrosion resistance after FSP. Peat et al. (Ref 25) investigated the erosion performance of the cold-sprayed WC-CoCr, Cr$_3$C$_2$-NiCr, and Al$_2$O$_3$ coatings on AA5083 substrate after FSP, and showed that a uniform dispersion of the reinforcement particles drastically dropped the volume loss of the spray-stirred surfaces. Moreover, Khodabakhshi et al. (Ref 26) carried out FSP to improve the cold-sprayed Al coatings on Mg alloy substrate, resulting in the dense and homogenous coatings and the formation of the intermixed layers due to the solid-state diffusion between the Al coating and Mg substrate.

It should be noted that the study of the FSWed Al/Mg joints is instructive for that of the FSPed Al coating on Mg substrate. Sato et al. (Ref 27) used FSW to join 1050 Al and AZ31 Mg alloys, where the Al$_{12}$Mg$_{17}$ intermetallic compound (IMC) was formed from the constitutional liquation in the weld center. Chen et al. (Ref 28) reported the lap joining of Al-Si and Mg-Al-Zn alloys by FSW, showing that the Al$_{12}$Mg$_{17}$, Al$_3$Mg$_2$ and Mg$_2$Si IMCs were generated in the joint. Kostka et al. (Ref 29) joined AA6040 Al alloy to AZ31 Mg alloy by FSW and showed that the nanocrystalline Al$_3$Mg$_2$ phase was adjacent to the Al$_{12}$Mg$_{17}$ layer in the AA6040 Al alloy. Firouzdor et al. (Ref 30) discussed the lap and butt FSW of 6061-T6 Al and AZ31B-H24 Mg alloys, observing that the Al$_3$Mg$_2$ and Al$_{12}$Mg$_{17}$ phases were formed near the Al and Mg sides, respectively. In addition, the presence of the eutectic structure and solidified droplets between the Al and Mg plates were the evidence of the liquid formation during FSW.

Obviously, the IMCs are usually generated from the liquid phase in the FSWed Al/Mg joints. However, only few studies have reported similar results of the FSPed Al coating on Mg substrate. Thus, future studies are still required to understand the formation of the IMCs and the effect of the IMCs within the coating on the hardness and corrosion resistance of the cold-sprayed Al coating after FSP. It is well known that cold spraying can prepare coatings on curved surfaces (Ref 31, 32). Compared with FSP (Ref 33), multi-spot friction stir-spot-processing (FSSP) is more flexible to handle the coatings on these surfaces. During multi-spot FSSP, the processed area covers the whole coating surface by multiple spots, which improves the overall performance of the coating. However, to understand the microstructure and properties of the coating processed by multi-spot FSSP, it is necessary to understand the effect of a single spot on the coating. Therefore, FSSP was introduced to modify the cold-sprayed Al coating on AZ91D substrate in this study. The formation of the IMCs in the cold-sprayed Al coating on AZ91D substrate after FSSP was studied in detail, and the influence of the IMCs on the microhardness and corrosion resistance was discussed.

Experimental Section

Commercially available pure Al particles, with an average size of 35 μm, were used as the spraying powder. The powder morphology is shown in Fig. 1(a). The grit-blasted AZ91D Mg alloy was used as the substrate (40 × 40 × 3 mm). A cold spray system (CS-2000, Xi'an Jiaotong University, China), equipped with a convergent-divergent nozzle, was employed to deposit the desired coating. Nitrogen was used as the driving gas at a pressure of 3 MPa and a temperature of 230°C. The standoff distance was 20 mm. The spraying gun was traversed relative to the substrate at 40 mm/s. The powder feeding rate was set at 30 g/min. To ensure the identical specimen thicknesses, the as-deposited coatings were ground to around 1.5 mm before FSSP.

The as-deposited coating was processed using a friction stir welding machine (LQH-G15, Weihai Lian Qiao Precision Machinery Co., Ltd., China). During FSSP, the tool rotation speeds of 2100, 2400, 2700, and 3000 rpm were performed, respectively. The plunge rate, plunge depth, and dwelling time were set at 1 mm/min, 0.5 mm, and 5 s, respectively. A pin-less H13 steel tool, with a diameter of 16 mm, was employed to modify the coating, and six involute grooves were machined on the tool surface, as given in Fig. 1(b).
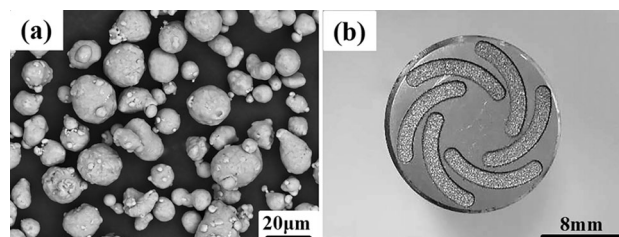

Fig. 1 (a) Powder morphology and (b) tool surface

Then, the FSSPed Al coatings were cut, ground, and polished for metallographic observations. The macrostructure of the coatings after FSSP at different rotation speeds was investigated by optical microscopy (OM, Nikon MA200, Japan). The microstructures of the FSSPed Al coatings were observed by scanning electron microscopy (SEM, MIRA 3 LMH, TESCAN, Czech), equipped with an electron backscatter diffraction (EBSD) system (Nordlys-Nano, Oxford, UK). The elemental compositions at different locations in the cold-sprayed Al coating on AZ91D substrate after FSSP were analyzed by energy-dispersive x-ray spectroscopy (EDS, Aztec, UK). For EBSD examination, the samples were prepared using an ion polisher (Leica EM RES102, China) after mechanical polishing. An electron backscatter diffraction detector (Symmetry, Oxford, UK) was employed to index the types and distributions of the IMCs and examine the crystallographic orientations between different phases. The acceleration voltage and step size were set to 20 keV and 300 nm, respectively. The crystal structure data, used to detect the $Al_{12}Mg_{17}$ phase, were included in the EBSD system, while the crystal structure data of Al_3Mg_2 was obtained from (Ref 34). The external reference frame was defined by the transverse direction (TD) and normal directions (ND), which can be seen in Fig. 6(a). A Vickers hardness indenter machine (Buehler 5103, USA) was used to measure the microhardness in the cold-sprayed Al coating on AZ91D substrate under the load of 100 gf for a 10 s dwell time.

The corrosion behavior of the coatings was probed by potentiodynamic polarization using an electrochemical workstation (CS310, Corrtest Instruments Co., Ltd, Wuhan, China) with a classical three-electrode electrochemical cell. The platinum electrode was employed as the counter electrode, and the saturated calomel electrode (SCE) was utilized as the reference electrode. The coated samples before and after FSSP, with an exposed surface of 2 cm^2, were performed as the working electrode. The sample surfaces were polished before the electrochemical testing, and at least three samples were used to study the corrosion behavior. As the electrolyte, 3.5 wt.% NaCl aqueous solution was used, and the potentiodynamic polarization was performed in the voltage range of -0.7 to +0.7 V at the scan rate of 0.5 mV/s at room temperature. For comparison, the tests were also performed on the pure Al bulk and AZ91D substrate.

Results and Discussions

Macrostructure of Cold-Sprayed Coatings on AZ91D Substrate after FSSP

The surface appearances and cross sections of the cold-sprayed Al coatings on AZ91D substrate after FSSP at different rotation speeds are shown in Fig. 2. The processed coating was divided into three zones, namely the border zone, 1/2 radius zone, and center zone, which are marked in Fig. 2(b). Figure 2(a) and (b) shows that the coating was detached from the substrate at the rotation speed of 2100 rpm due to the insufficient heat input. Therein, the interface between the cold-sprayed coating and substrate maintained the mechanical interlocking with poor bonding strength. Figure 2(c) and (f) gives that the sound cold-sprayed Al coatings on AZ91D substrates were obtained at the appropriate rotation speeds of 2400 and 2700 rpm. Figure 2(d) and (f) shows a sharp brightness contrast between the upper part of the 1/2 radius zone and center zone in the processed coating, which could be attributed to the more intense material flow in the upper part of the 1/2 radius zone (Ref 35). Considerable IMCs with a thickness of about 300 μm were observed at the interface in the 1/2 radius area, which was related to the formation of the liquid phase. Moreover, the IMCs named as "strip" extended from the edge of the thick IMCs to the border of the coating surface as shown in Fig. 2(f), indicating that the liquid phase was squeezed into the coating during FSSP. Figure 2(h) demonstrates a hunch-up defect in the unprocessed zone at the rotation speed of 3000 rpm, suggesting that the excessive liquid phase was formed at the interface, and entered the coating through the weak bonding positions between the particles to reach the unprocessed zone. Moreover, the band structure appeared in the processed coating, which extended from the thick IMCs to the center of the coating surface. Similar to FSSW, the material flow is generated in the coating during FSSP and increases with the increase of the rotation speed (Ref 35-37). Therefore, when the enhanced material flow reached the interface, the liquid phase will mix and react with the coating to form the band structure.

Microstructures of Cold-Sprayed Al Coating on AZ91D Substrate after FSSP

Microstructures of Cold-Sprayed Al Coating after FSSP

Figure 3 shows the microstructures and element distributions of the unprocessed zone and processed coating in different zones at 2700 rpm. Figure 3(a) presents that abundant pores appeared in the as-deposited coating. As shown in Fig. 3(d), (g), (j), (m), and (p), these evident pores almost completely disappeared in different zones of the processed coating due to the forging effect of the tool (Ref 19). However, different zones in the processed coating showed different microscopic morphologies. Figure 3(m) and (p) presents that a few tiny pores appeared in the lower part of the 1/2 radius and center zones, which is related to the temperature gradient generated within the

coating during FSSP (Ref 38). In addition, Mg element was found in the upper part of the 1/2 radius zone as shown in Fig. 3(l), which is the result of the liquid phase entering the interior of the coating. In contrast, Mg elements were absent in the lower part of the 1/2 radius zone as given in Fig. 3(o), indicating that the liquid phase did not directly pass through the lower part of the coating into the upper part of the coating. This result can be attributed to the material flow pattern during FSSP. When the liquid phase formed at the interface between the coating and substrate was squeezed to the border of the coating surface, the grooves on the tool surface promoted it to flow toward the center of the coating surface (Ref 38). Once the liquid phase reached near the 1/2 radius of the coating surface, it flowed downward with the material flow and mixed with the coating.

Microstructures of Interfacial Structures Between Coating and Substrate

Figure 4 shows the interfacial structure of the unprocessed area and center area after FSSP at 2700 rpm. Figure 4(b) and (e) shows that the shape of the interface changed from wavy to smooth in the center area after FSSP, and the thin IMCs with about 7 μm thick were found. The corresponding EDS results are shown in Table 1. As given in Fig. 4(f), the thin IMCs were divided

Fig. 3 Microstructures and elemental distributions of (a-c) the ▶ unprocessed zone and processed coating in the upper part of the border zone (d-f); lower part of the border zone (g-i); upper part of the 1/2 radius zone (j–l); lower part of the1/2 radius zone (m–o); and center zone at 2700 rpm

into two layers. The layer near the Al coating was mainly composed of Al_3Mg_2, while the layer near the AZ91D substrate was mainly composed of $Al_{12}Mg_{17}$. Meanwhile, the $(Mg)_{SS}$ was found in the $Al_{12}Mg_{17}$ layer. The mixed structure of $Al_{12}Mg_{17}$ and $(Mg)_{SS}$ indicated that the IMCs at the interface in the center area were formed from the liquid phase.

Figure 5 shows the interfacial structure in the 1/2 radius area. Figure 5(a) gives that the thick IMCs were divided into the bright and dark parts, indicating an uneven component distribution. The dark part was smaller than the bright part and was predominantly located at both ends and the bottom of the thick IMCs. Furthermore, the dark part also appeared in the middle of the thick IMCs and extended from the substrate to the coating. This phenomenon is related to the higher temperature in this area during FSSP (Ref 38).

Then, the thick IMCs were analyzed from the right to the left side. As shown in Fig. 5(b), at the right end, the interfacial structure was similar to the center area of the
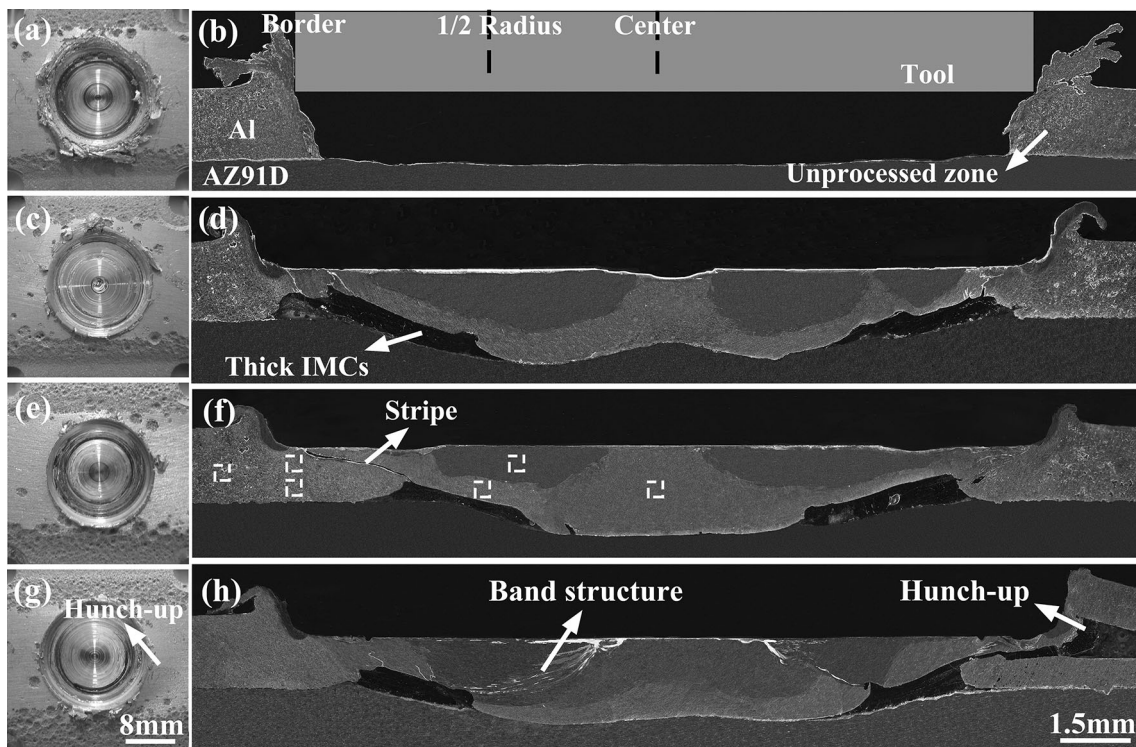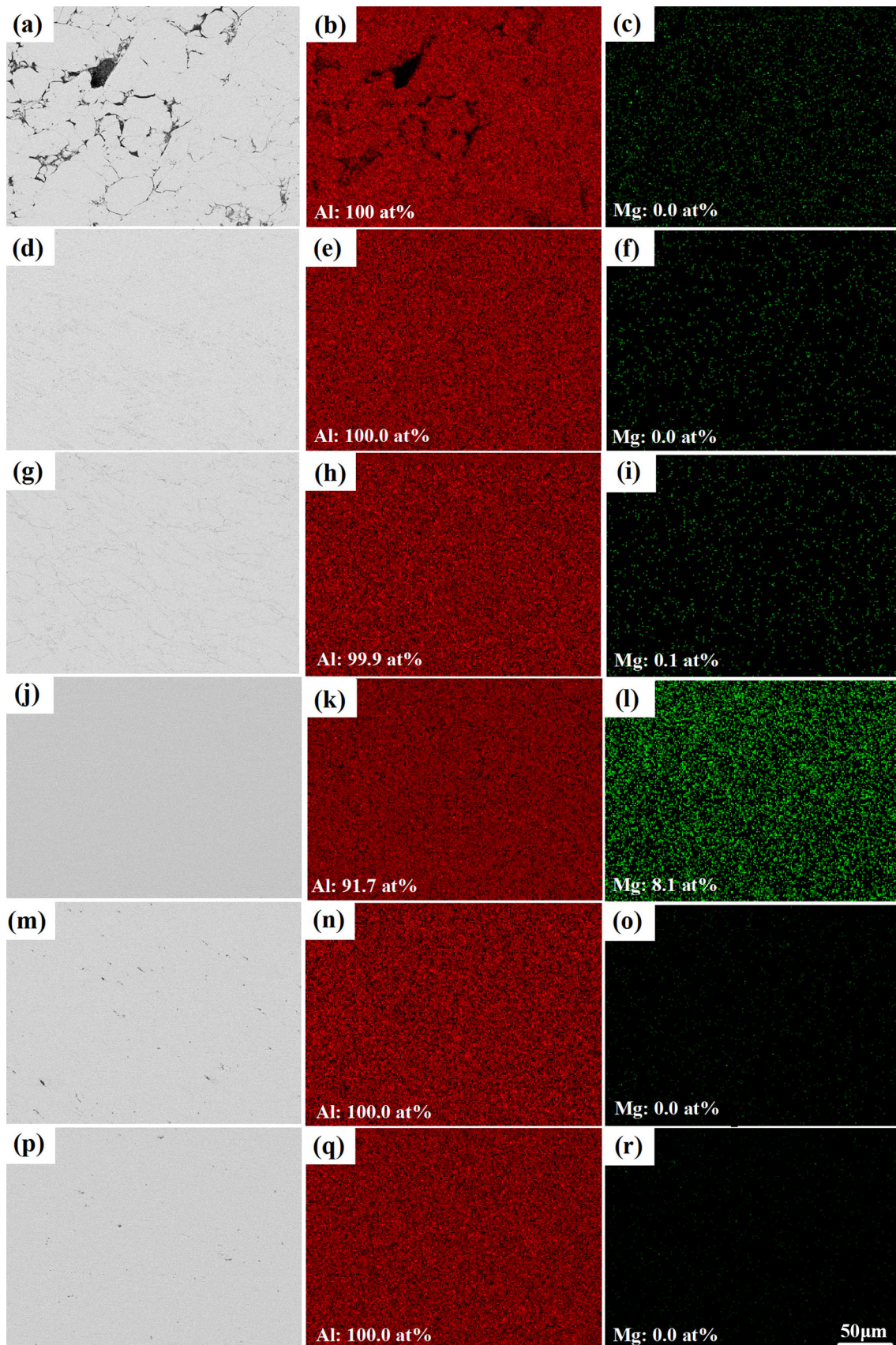

Fig. 2 Surface appearances and cross sections of the cold-sprayed Al coatings on AZ91D substrate after FSSP at different rotation speeds: (a, b) 2100 rpm; (c, d) 2400 rpm; (e, f) 2700 rpm; (g, h) 3000 rpm

Al: 100 at%

Mg: 0.0 at%

Al: 100.0 at%

Mg: 0.0 at%

Al: 99.9 at%

Mg: 0.1 at%

Al: 91.7 at%

Mg: 8.1 at%

Al: 100.0 at%
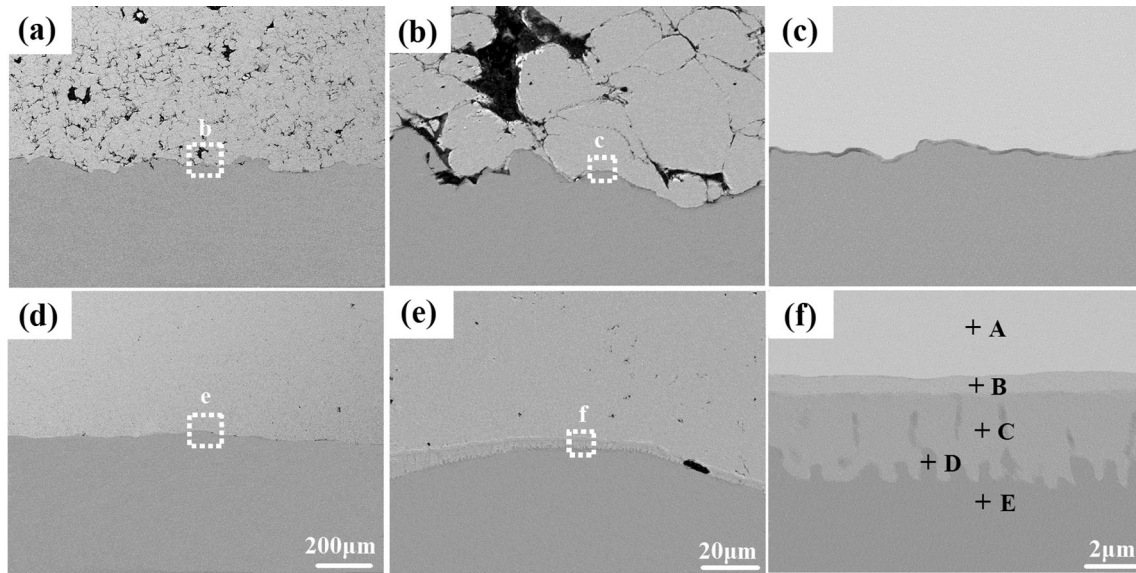
Mg: 0.0 at%

Al: 100.0 at%

Mg: 0.0 at%

50μm

Fig. 4 Interfacial structure in: (a-c) unprocessed area and (d-f) center area after FSSP at 2700 rpm

Table 1 EDS results of different locations in the interface between the cold-sprayed Al coating and AZ91D substrate after FSSP at 2700 rpm

Areas	Locations	Elements/at.%		Possible phases
		Al	Mg	
Thin IMCs in the center	A	99.4	0.6	Al coating
	B	61.7	38.3	Al_3Mg_2
	C	36.1	63.9	$Al_{12}Mg_{17}$
	D	21.1	78.9	$(Mg)_{SS}$
	E	3.2	96.8	AZ91D
Thick IMCs in the 1/2 radius	F	65.1	34.9	Al_3Mg_2
	G	38.4	61.6	$Al_{12}Mg_{17}$
	H	29.7	70.3	$(Al_{12}Mg_{17}+Mg)$ eutectic structure
	I	37.3	62.7	$Al_{12}Mg_{17}$
	J	21.8	78.2	$(Mg)_{SS}$
	K	62.0	38.0	Al_3Mg_2
	L	46.2	53.8	$Al_{12}Mg_{17} +Al_3Mg_2$
	M	38.1	61.9	$Al_{12}Mg_{17}$
	N	16.1	83.9	$(Mg)_{SS}$
	O	61.4	38.6	Al_3Mg_2
	P	43.0	57.0	$Al_{12}Mg_{17} +Al_3Mg_2$
	Q	62.1	37.9	Al_3Mg_2
	R	60.7	39.3	Al_3Mg_2

thin IMCs. The side near the Al coating was mainly constituted by the Al_3Mg_2 layer, while the side near the AZ91D substrate was mainly constituted by the $Al_{12}Mg_{17}$ layer, in which a small amount of $(Mg)_{SS}$ island structure was found. Fig. 5(c) and (d) shows that numerous large-sized $Al_{12}Mg_{17}$ island structures were trapped within the $(Al_{12}Mg_{17}+Mg)$ lamellar eutectic structure. This indicates that the component of the initial liquid phase was present within the $(Al_{12}Mg_{17}+Mg)$ hypoeutectic region. However, the $(Al_{12}Mg_{17}+Mg)$ lamellar eutectic structure was almost replaced by the small $(Mg)_{SS}$ island structure near the AZ91D substrate. As the composition of the liquid phase contained in this area was located in the $(Al_{12}Mg17+Mg)$ hypoeutectic region, the $Al_{12}Mg_{17}$ phase will preferentially precipitate from the liquid phase (Ref 39). Then, the morphology between the $Al_{12}Mg_{17}$ phases are related to
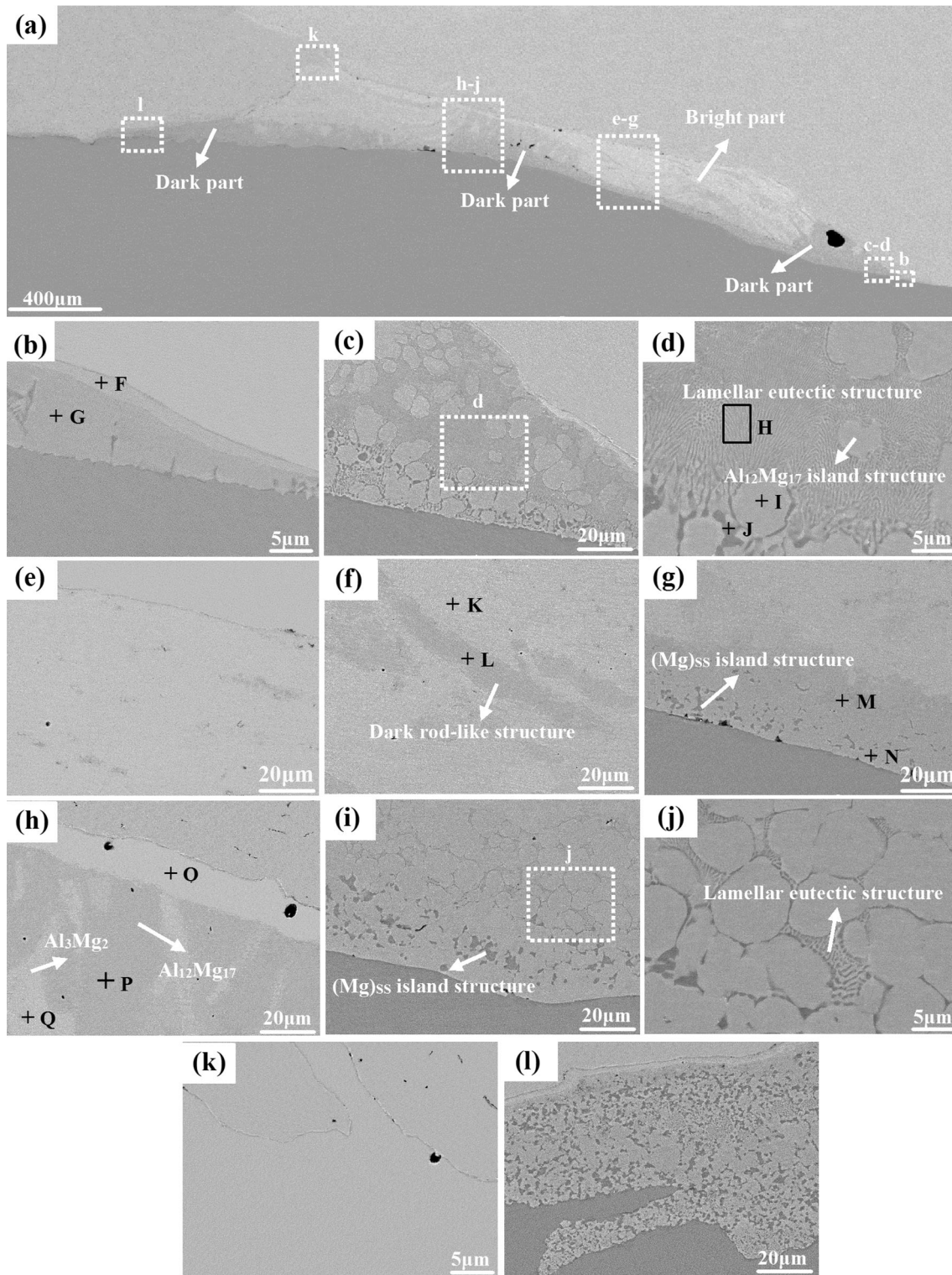
Fig. 5 Interfacial structure in the 1/2 radius area after FSSP at 2700 rpm: (a) macrostructure; (b-l) microstructure

the cooling rate (Ref 40). Generally, the diffusion of atoms determines the growth of the eutectic structure (Ref 40). When the cooling rate is not very high, the Al and Mg atoms have enough time to diffuse, and the eutectic structure will be formed between the $Al_{12}Mg_{17}$ island structures. However, at a high cooling rate, the diffusion between the Al and Mg atoms is inhibited, and only $(Mg)_{ss}$ island structure will be generated between the $A_{12}Mg_{17}$
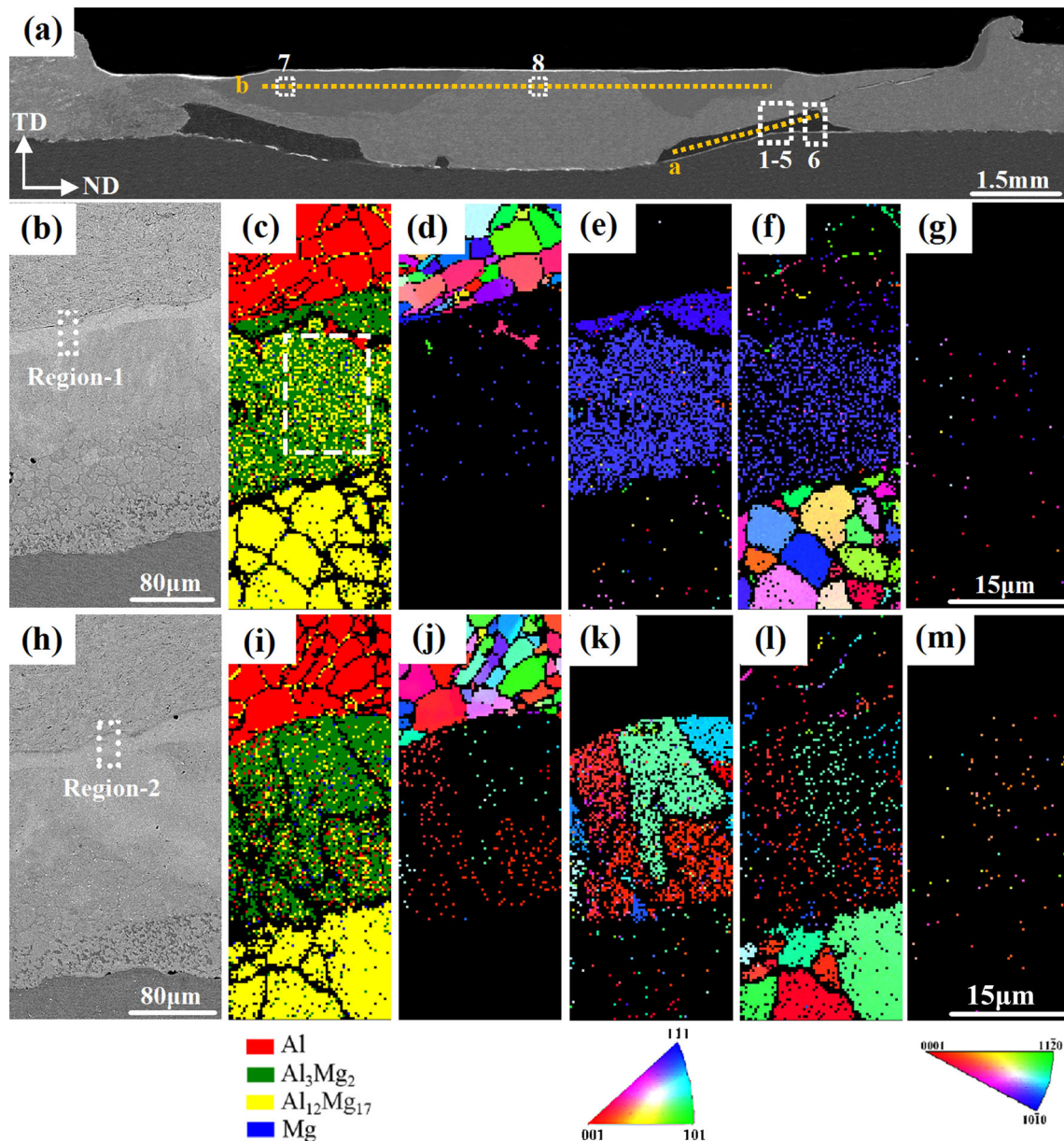
Fig. 6 (a) Locations selected for EBSD and hardness analyses, and the phase distributions of (b-g) region-1 and (h-m) region-2 in the middle of the thick IMCs near the Al coating side.

island structures. Figure 5(e) and (f) shows a dark rod-like structure in the bright part. The EDS analysis revealed that the bright part was mainly composed of Al_3Mg_2. A higher Al content was measured in the dark rod-like structure compared to $Al_{12}Mg_{17}$. Therefore, it is speculated that the dark rod-like structure may be the mixed structure of $Al_{12}Mg_{17}$ and Al_3Mg_2. Figure 5(g) shows that the dark part was present near the substrate, which was identified as the mixed structure of $Al_{12}Mg_{17}$ and $(Mg)_{SS}$. Figure 5(h) presents the microstructure of the dark part in the middle of the thick IMCs, revealing that the Al_3Mg_2 layer appeared near the Al coating side, while the mixed structure of

$Al_{12}Mg_{17}$ and Al_3Mg_2 was found beneath it. As given in Fig. 5(i) and (j), a smaller amount of $(Al_{12}Mg_{17}+Mg)$ lamellar eutectic structure was observed among the large-sized $Al_{12}Mg_{17}$ island structures, which was replaced by $(Mg)_{SS}$ near the Mg substrate. Figure 5(k) displays that the bright part and the strip were mainly composed of Al_3Mg_2 in the upper left side of the thick IMCs. As shown in Fig. 5(j), the left end of the thick IMCs was composed of $Al_{12}Mg_{17}$, $(Mg)_{SS}$, and a smaller amount of $(Al_{12}Mg_{17}+Mg)$ eutectic structure.

Different dimensions at the interface in different areas of the IMCs are mainly related to the temperature distribution
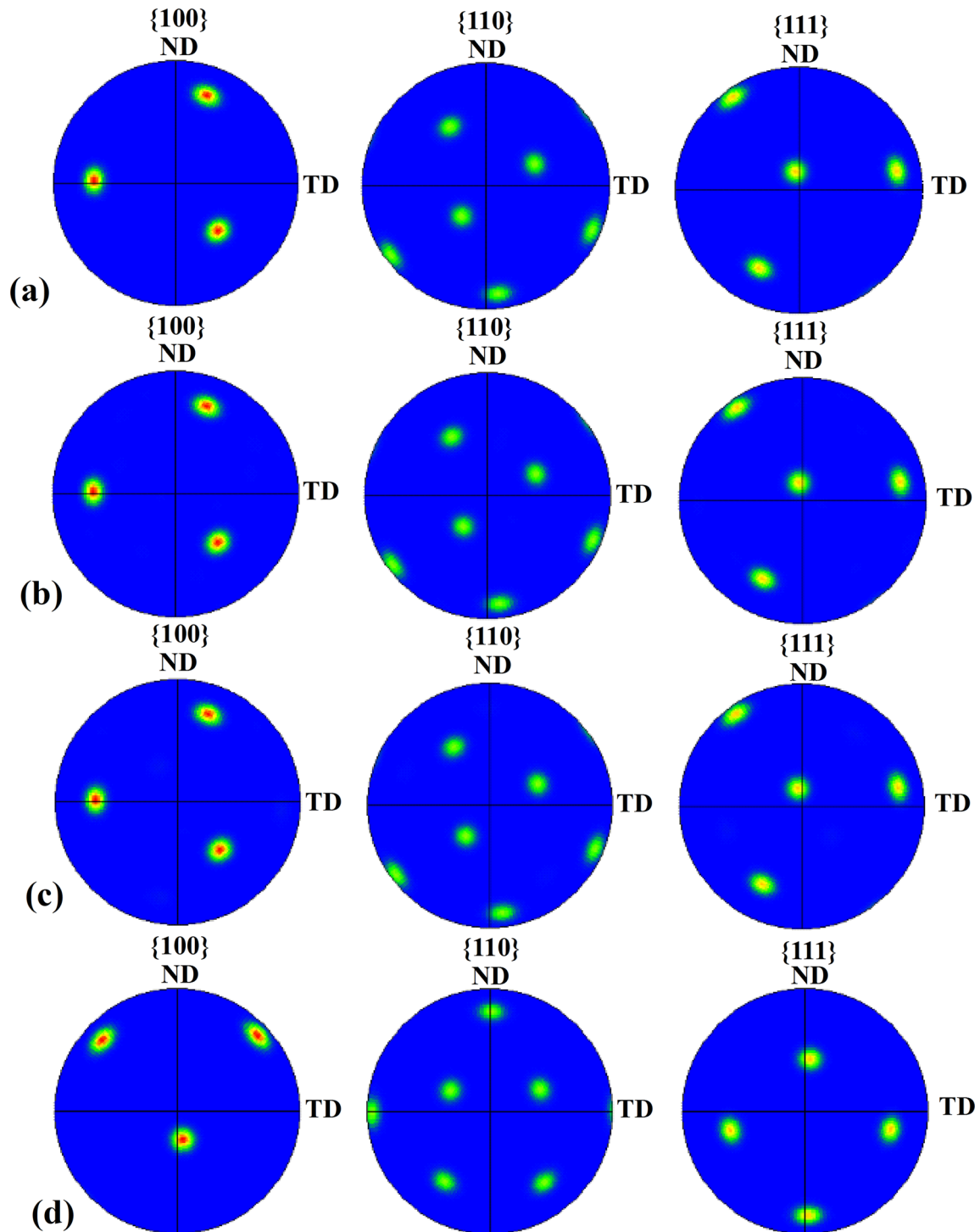
Fig. 7 Pole figures of (a) fine Al grains, (b) Al_3Mg_2 grains, (c) $Al_{12}Mg_{17}$ grains, and (d) large-sized Al grains in the white rectangle of the phase map in region-1

in the coating during FSSP. It is well known that the border of the tool generates the most heat due to the highest linear velocity. However, some of the heat dissipates into the surroundings. Therefore, the highest temperature area shifted inward to the area around the 1/2 radius of the tool

due to heat accumulation (Ref 38), which allowed a large amount of liquid phase to be generated at the interface around the 1/2 radius area. Another reason is that the liquid phase generated at the interface in the center area is squeezed to the 1/2 radius area due to the forging effect of
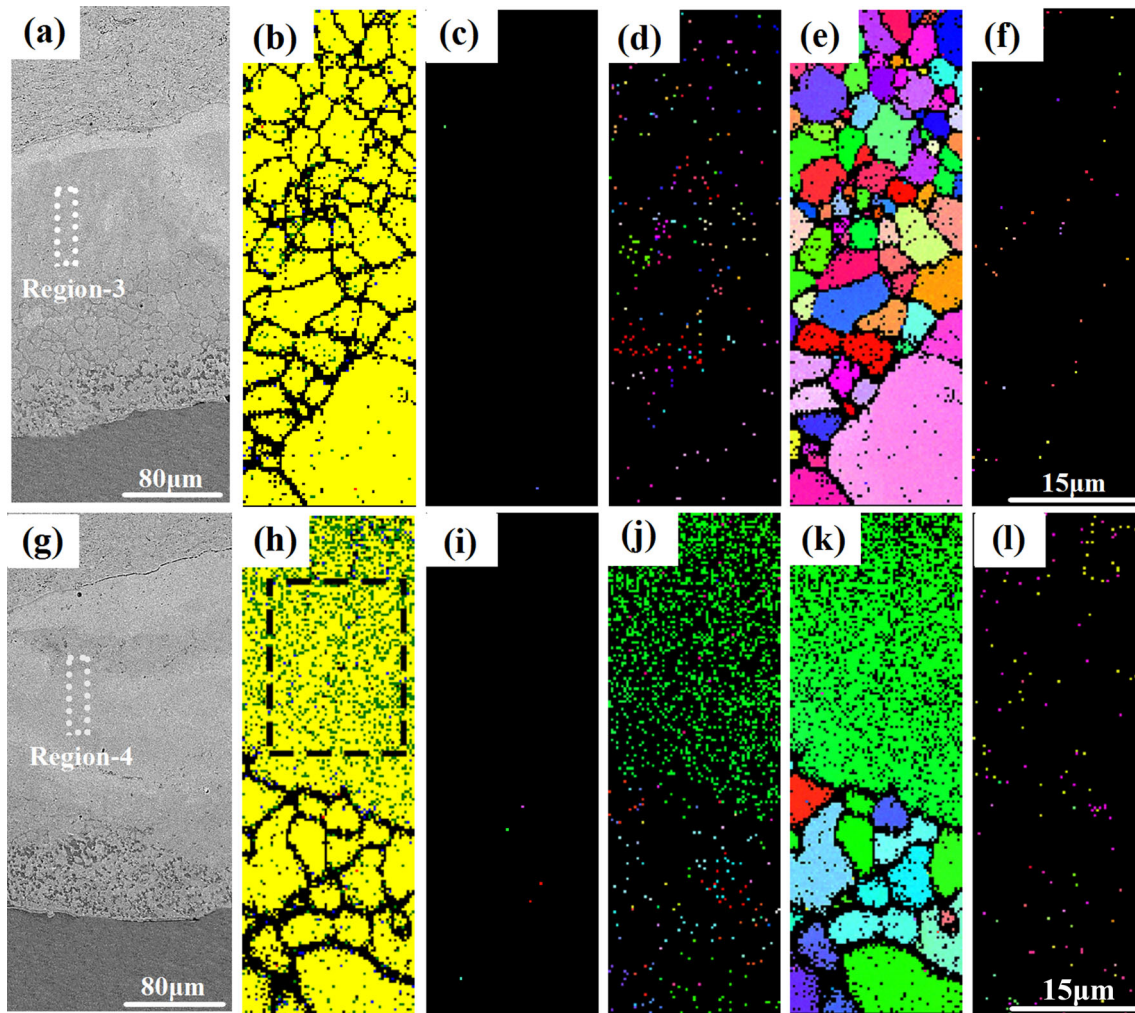
Fig. 8 Phase distributions of (a-f) region-3 and (g-l) region-4 in the middle of the thick IMCs beneath the four-phase coexistence structure layer.

the tool, which further increased the liquid phase at the interface in the 1/2 radius area.

Phase Distributions in the Cold-Sprayed Al Coating on AZ91D Substrate after FSSP

Figure 6(a) shows the locations selected for EBSD and hardness analyses. These analyses were performed on the other half of the sample processed at 2700 rpm. Fig 6(b)-(m) displays the phase distributions of region-1 and region-2, which were located in the dark part and dark-bright boundary part in the middle of the thick IMCs near the Al coating side, respectively. Figure 6(c) and (i) shows that four phases coexisted in these regions, which were dominated by Al_3Mg_2. Figure 6(d)-(g) and (j)-(m) presents that a large amount of fine $Al_{12}Mg_{17}$ phase, a small amount of fine Al phase, and a trace amount of fine Mg phase were dispersed and embedded in the Al_3Mg_2 phase. This result indicates that the initial liquid phase was unevenly mixed

and reacted with a large number of Al particles after entering the coating, so that the composition of the final liquid phase was inhomogeneously distributed between the $(Al+Al_3Mg_2)$ hypereutectic region and $(Al_{12}Mg_{17}+Mg)$ hypoeutectic region. Moreover, it can be seen from Fig. 6(d)-(f) and Fig. 6(j)-(l) that the Al, Al_3Mg_2, and $Al_{12}Mg_{17}$ grains had the same crystallographic orientation in this four-phase coexistence structure.

The pole figures of the typical positions of the phases in region-1 are shown in Fig. 7. The cubic-to-cubic orientation relationship was found between the Al and Al_3Mg_2 grains. This orientation relationship has been established between the Al and Al_3Mg_2 grains at interface between the 1060 aluminum alloy and AZ31B magnesium alloy after multi-pass FSP, which lowers the interfacial energy (Ref 41). In addition, the same orientation relationship was found between the Al_3Mg_2 and $Al_{12}Mg_{17}$ grains. Even though the orientation relationship between FCC and BCC structures was usually described as the Kurdjumov-Sachs
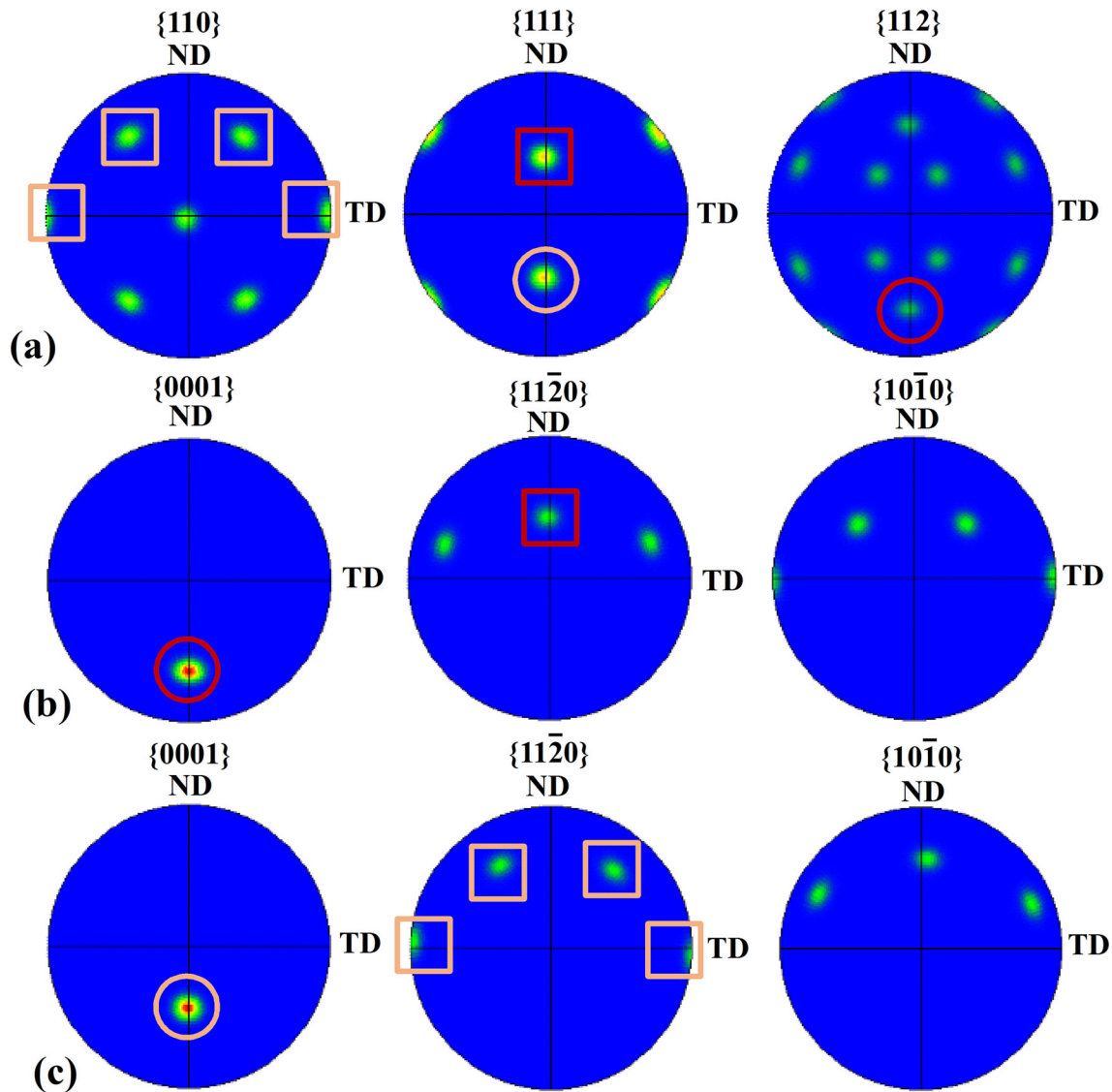
Fig. 9 Pole figures of (a) $Al_{12}Mg_{17}$, (b) fine Mg grains, and (d) fine Mg grains with another orientation in the black rectangle of the phase map in region-4

(KS) or Nishiyama-Wassermann (NW) relationship, the cubic-to-cubic orientation relationship was also found between austenite (FCC) and ferrite (BCC) grains (Ref 42-44). In addition, as given in Fig. 6(d), large-sized Al grains were trapped in the IMCs layer near the Al coating side, which had a different orientation from the fine Al grains. Furthermore, as given in Fig. 7(a) and (d), no orientation relationship was found between the large-sized Al grains and Al_3Mg_2 grains. This result suggests that the large-sized Al grains were still present due to the incomplete reaction of the Al particles during FSSP.

Figure 8 shows the phase distributions of region-3 and region-4, which were located in the dark part and dark-bright boundary part in the middle of the thick IMCs, respectively. As given in Fig. 8(b)-(f) and (h)-(l), the three-phase coexistence structure dominated by $Al_{12}Mg_{17}$ was found in these two regions. Furthermore, a small amount of fine Al_3Mg_2 grains and a trace amount of fine Mg grains were dispersed and embedded in the $Al_{12}Mg_{17}$ grains, as only a small amount of particles were mixed with the initial liquid phase in these regions, the composition of the final liquid phase was still in the ($Al_{12}Mg_{17}$+Mg) hypoeutectic region. Compared with Fig. 8(d) and (j), the content of Al_3Mg_2 in region-4 was higher than that in region-3, suggesting that region-4 involved more Al elements. Moreover, comparisons between Fig. 8(d), (e), and (j), (k) showed that the crystallographic orientations of the Al_3Mg_2 grains and $Al_{12}Mg_{17}$ grains were the same, which indicated a cubic-to-cubic orientation relationship between the Al_3Mg_2 and $Al_{12}Mg_{17}$ grains in these regions.
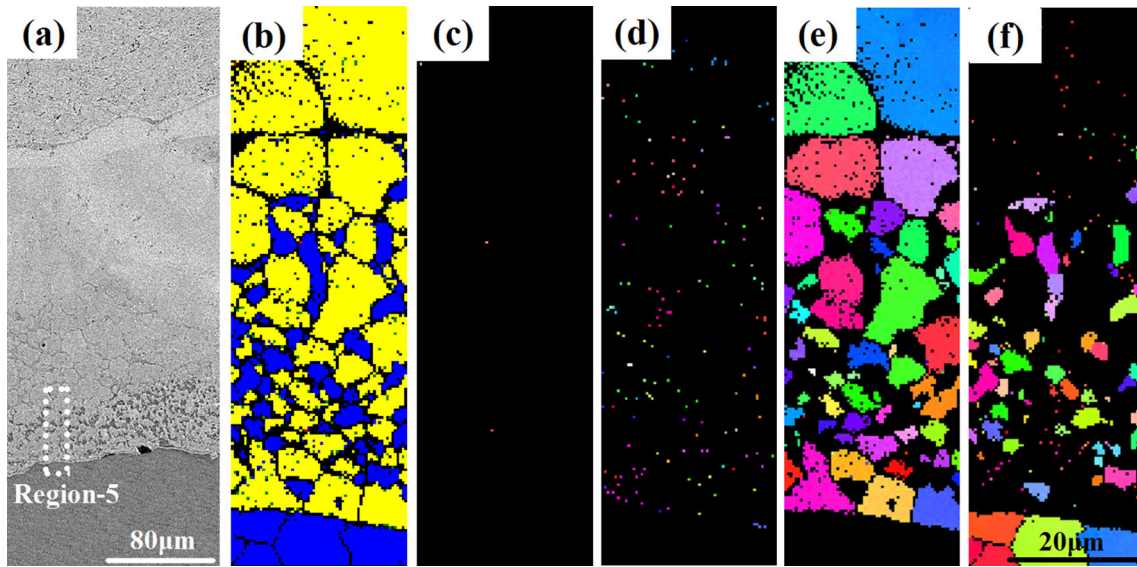
Fig. 10 Phase distribution of region-5 in the middle of the thick IMCs near the AZ91D substrate
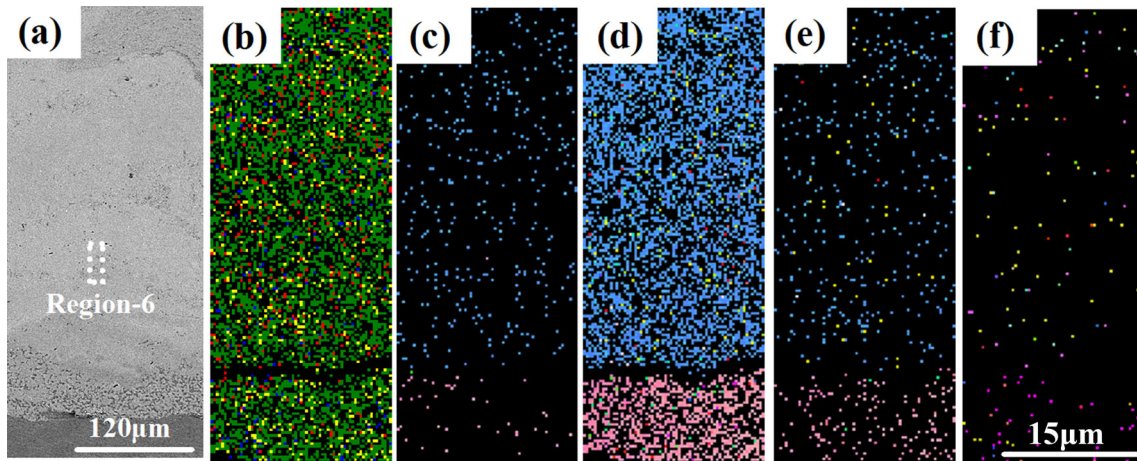

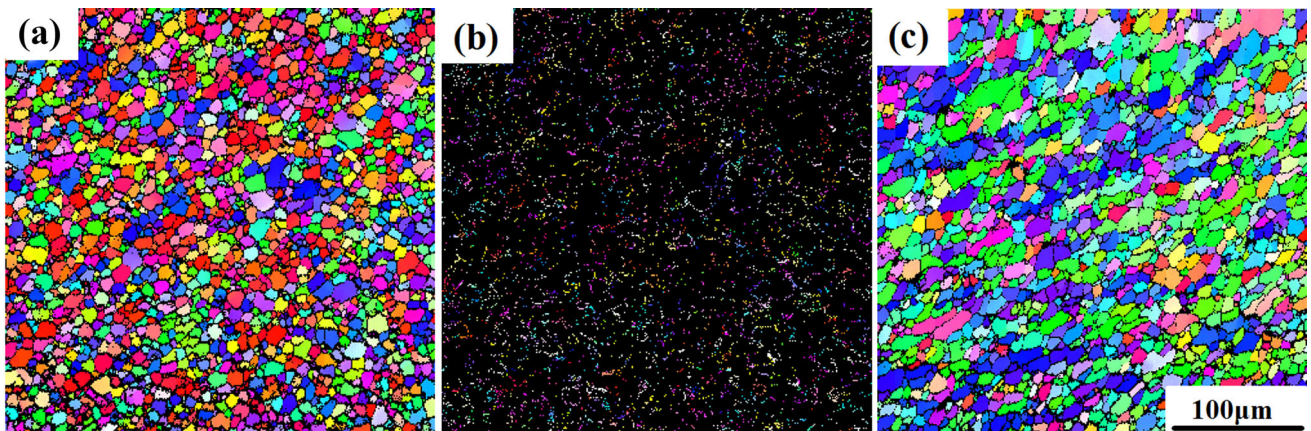**Fig. 11** Phase distribution of region-6 in the typical bright part of the thick IMCs

Fig. 12 EBSD results of (a, b) upper part of the 1/2 radius zone and (c) center zone in the processed coating at 2700 rpm
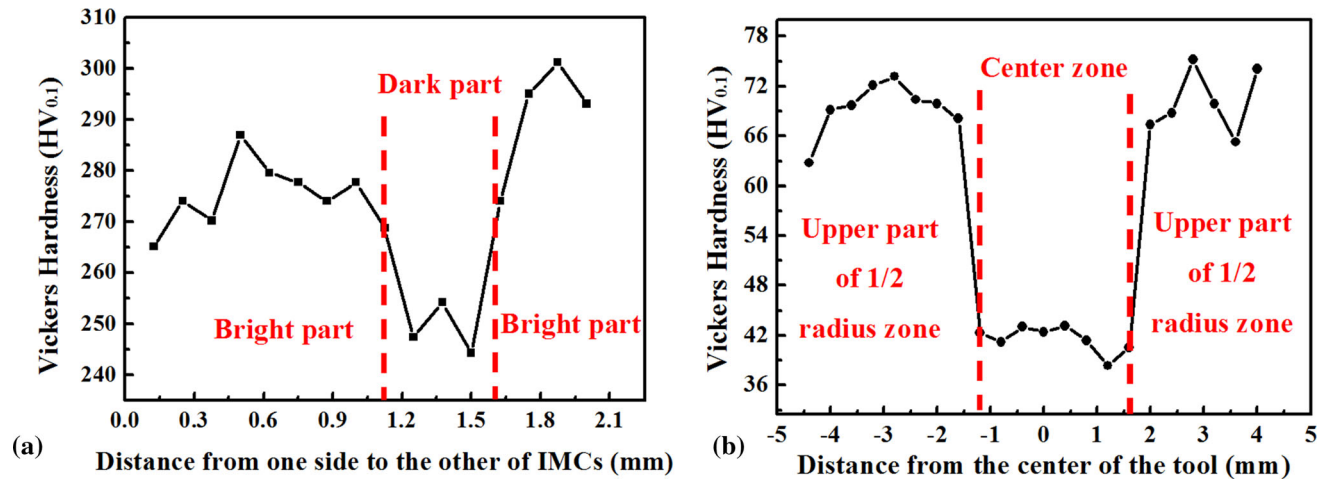
Fig. 13 Microhardness distributions of the (a) thick IMCs and (b) processed coating at 2700 rpm
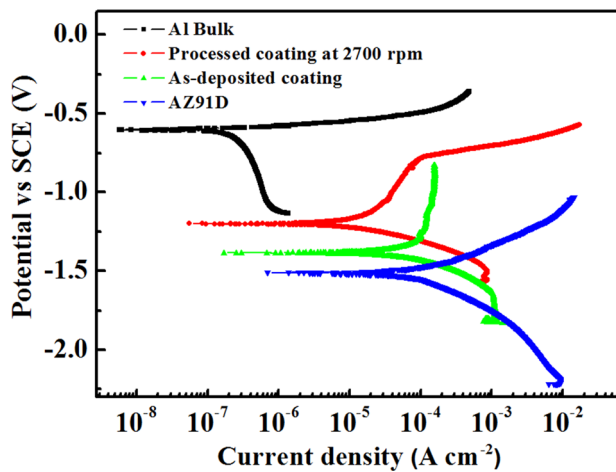

Fig. 14 Comparison of the potentiodynamic polarization vs. current density of the as-deposited coating, processed coating at 2700 rpm, AZ91D substrate, and pure Al bulk

Table 2 Corrosion potential and corrosion current density of the samples obtained after potentiodynamic polarization

Samples	E_{corr}/V	I_{corr}/A cm^{-2}
Al bulk	−0.64	1.85E−7
Processed coating at 2700 rpm	−1.19	4.87E−6
As-deposited coating	−1.39	4.43E−5
AZ91D	−1.51	9.46E−5

Figure 8(k) and (l) reveals that one $Al_{12}Mg_{17}$ crystallographic orientation corresponded to two Mg crystallographic orientations within an $Al_{12}Mg_{17}$ grain.

Figure 9 shows the pole figures of the $Al_{12}Mg_{17}$ grains and Mg grains selected from region-4. Two distinct orientation relationships were observed between the $Al_{12}Mg_{17}$ and Mg grains. The first orientation relationship between the $Al_{12}Mg_{17}$ grains and Mg grains was the OR9

relationship (Ref 45), i.e., $(1\bar{2}1)$ $_{Al12Mg17}$ // (0001) $_{Mg}$, $[11\bar{1}]$ $_{Al12Mg17}$ // $[1\bar{2}10]$ $_{Mg}$. The second orientation relationship between the $Al_{12}Mg_{17}$ and Mg grains was found to be (111) $_{Al12Mg17}$ // (0001) $_{Mg}$, $[10\bar{1}]$ $_{Al12Mg17}$ // $[11\bar{2}0]$ $_{Mg}$.

Figure 10 shows the phase distribution of region-5, which was located in the middle of the dark part of the thick IMCs near the AZ91D substrate. The three-phase coexistence structure dominated by $Al_{12}Mg_{17}$ was the main structure, and the $(Mg)_{SS}$ island structure appeared between the three-phase coexistence structure near the AZ91D substrate. However, the unrecognized region was also found between the three-phase coexistence structures. According to Fig. 5(i) and (j), the unrecognized region was the $(Al_{12}Mg_{17}+Mg)$ lamellar eutectic structure.

Figure 11 exhibits the phase distribution of region-6, which was located in the typical bright part of the thick IMCs. It is found that the microstructure of this region was still the four-phase coexistence structure dominated by Al_3Mg_2.

Figure 12 shows the EBSD results of the processed coating in the upper part of the 1/2 radius and center zone, i.e., region-7 and region-8 given in Fig. 6(a), respectively. It should be noted that according to the EDS results presented in Fig. 3, four phases of Al, Al_3Mg_2, $Al_{12}Mg_{17}$, and Mg were chosen for the EBSD test of the upper part of the 1/2 radius zone, and only Al was chosen for the EBSD test of the center zone. Figure 12(a) and (b) reveals that a large amount of $Al_{12}Mg_{17}$ grains were distributed between the Al grain boundaries in the upper part of the 1/2 radius zone. However, Fig. 12(c) gives that the $Al_{12}Mg_{17}$ grains were absent in the center zone due to the liquid phase entering the coating. The formation of the $Al_{12}Mg_{17}$ phase is related to the interdiffusion of Al and Mg atoms. Since the diffusion activation energy of Al in Mg is higher than that of Mg
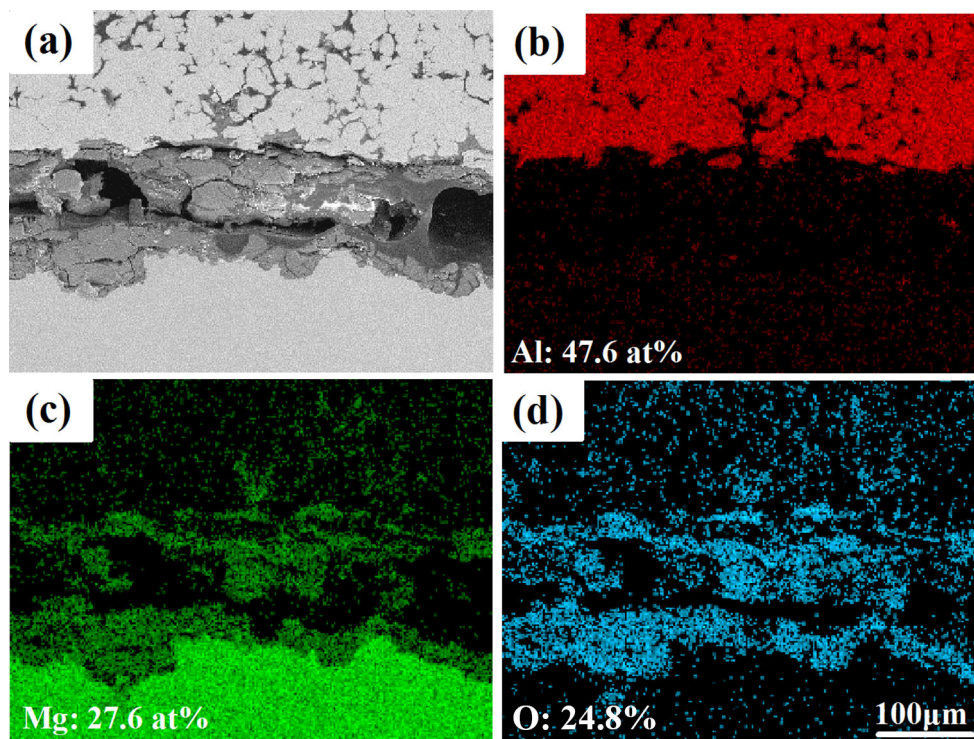
Fig. 15 Interface structure of the corroded coating before FSSP

in Al (Ref 46), $Al_{12}Mg_{17}$ containing more Mg elements was generated in the upper part of the 1/2 radius zone.

Effect of IMCs on Microhardness

Figure 13 shows the microhardness distributions of the thick IMCs and the processed coating at 2700 rpm. The locations selected for the microhardness tests are given in Fig. 6(a). Figure 13(a) shows the microhardness distributions of the thick IMCs. The microhardness in the bright part was around $280 \sim 300$ $HV_{0.1}$, while the microhardness in the middle of the dark part was around 245 $HV_{0.1}$. This result suggests that the microhardness in the four-phase coexistence structure dominated by Al_3Mg_2 was higher than that in the three-phase coexistence structure dominated by $Al_{12}Mg_{17}$, which is consistent with the results from Liu et al. (Ref 47) and Dietrich et al. (Ref 48). Figure 13(b) reveals the microhardness distributions of the center zone and upper part of the 1/2 radius zone in the processed coating. The microhardness in the center zone was about 43 $HV_{0.1}$, while the microhardness in the upper part of the 1/2 radius zone was sharply increased to about 70 $HV_{0.1}$. It is well known that the hard second-phases can extremely enhance the microhardness of materials (Ref 49, 50). Therefore, the large amount of dispersed $Al_{12}Mg_{17}$ phases significantly improved the microhardness in the upper part of the 1/2 radius zone.

Effect of IMCs on Corrosion Resistance

Figure 14 presents the potentiodynamic polarization curves of all test samples. The corrosion potentials (E_{corr}) and corrosion current densities (I_{corr}) derived from Fig. 14 are listed in Table 2. The AZ91D substrate had a high corrosion current density of 9.46E-5 A/cm^{-2}, while the as-deposited coating revealed a relatively lower corrosion current density of 4.43E-5 A/cm^{-2}. After FSSP, the corrosion current density of the coating was remarkably decreased to 4.87E-6 A/cm^{-2}. These results indicate that the processed coating provided more effective corrosion protection to the AZ91D substrate compared to the as-deposited coating. However, the corrosion current density of the processed coating was higher than that of the pure Al bulk, as listed in Table 2. As mentioned above (Fig. 12a and b), the $Al_{12}Mg_{17}$ grains appeared in the upper part of the 1/2 radius zone. Therefore, the galvanic corrosion of $Al_{12}Mg_{17}$ coupled with Al could be readily induced in the surface of the processed coating, leading to a higher corrosion current density of the processed coating compared to that of the pure Al bulk. This result is in good agreement with the corrosion resistance of the Al coating reinforced with $Al_{12}Mg_{17}$ particles (Ref 51).

To further illustrate the corrosion protection effect of the coatings to the AZ91D substrates before and after FSSP, the interfacial structures of the corroded coatings are given
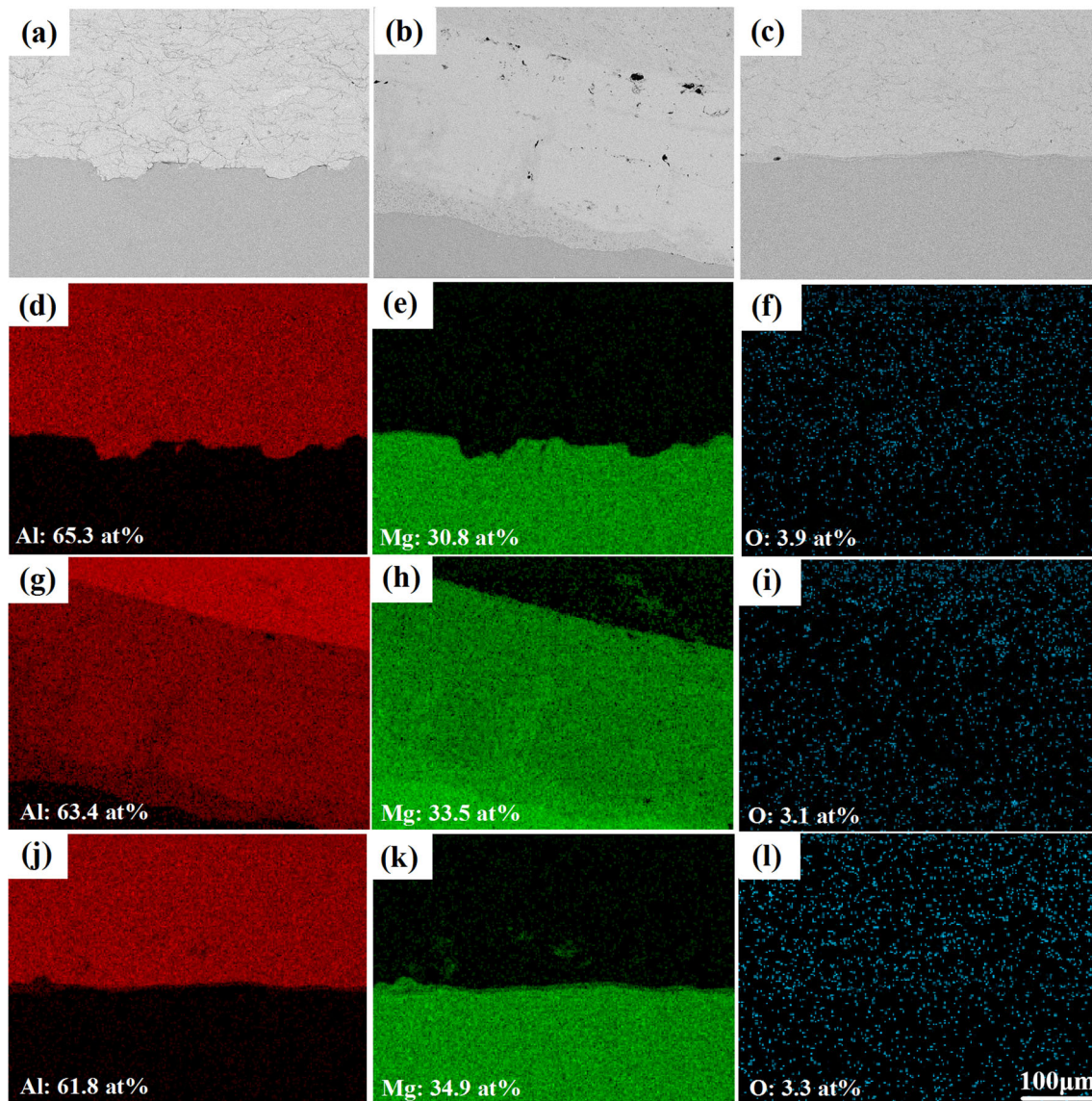
Fig. 16 Interface structures of the corroded coating in different areas after FSSP at 2700 rpm

in Fig. 15 and 16. Figure 15 shows that the corrosion product layer composed of Mg and O elements appeared at the interface of the as-deposited coating. In contrast, the corrosion product was absent at the interface in different areas after FSSP, as shown in Fig. 16. Due to the presence of the inter-particle interfaces in the cold-sprayed coating, the aqueous solution will enter the interior of the coating through the inter-particle interfaces, thus accelerating local corrosion (Ref 52, 53). Furthermore, even if the coating is very dense, the aqueous solution will reach the substrate through some inter-particle interfaces, causing corrosion to some areas of the substrate (Ref 54). However, the inter-particle interfaces within the coating were eliminated after FSSP, as shown in Fig. 3. Therefore, the corrosive solution could not reach the substrate to cause corrosion to the substrate, which means that the processed coating produced

effective corrosion protection to the substrate. In addition, as shown in Fig. 3 and 12, the IMCs only existed in the upper part of the 1/2 radius zone of the processed coating. The pure Al coating without IMCs was identified near the AZ91D substrate. When the upper part of the coating is consumed by corrosion, the corrosion mechanism of the bottom coating will change into general corrosion. At this time, the processed coating will still produce effective corrosion protection for the AZ91D substrate.

Conclusions

In summary, the main conclusions from the current researches are as follows:

(1) The coating detached from the substrate at 2100 rpm. The excessive liquid phase entered the interior of the coating in the unprocessed zone, leading to the hunch-up defect at 3000 rpm. The sound cold-sprayed Al coatings on AZ91D substrates were obtained at the rotation speeds of 2400 and 2700 rpm.

(2) The cold-sprayed Al coating became dense after FSSP. The thin IMCs were present at the interface in the center area, and the thick IMCs with complex morphology and structure were found at the interface in the 1/2 radius area. Furthermore, the eutectic structure was observed in the thick IMCs, indicating that the liquid phase was generated during FSSP.

(3) The three-phase coexistence structure and $(Mg)_{SS}$ island structure were present close to the substrate, while the $(Mg)_{SS}$ island structure was replaced by the eutectic structure distant from the substrate. The three-phase coexistence structure dominated by $Al_{12}Mg_{17}$ was mainly acquired in the middle of the thick IMCs. The four-phase coexistence structure dominated by Al_3Mg_2 occurred in the remaining region of the thick IMCs. Furthermore, the $Al_{12}Mg_{17}$ grains were present in the upper part of the 1/2 radius zone in the processed coating.

(4) Within the coexistence structures, the cubic-to-cubic orientation relationship was observed between the Al and Al_3Mg_2 grains, as well as between the Al_3Mg_2 and $Al_{12}Mg_{17}$ grains. Furthermore, in the three-phase coexistence structure, the orientation relationships between the $Al_{12}Mg_{17}$ and Mg grains were found to be $(1\bar{2}1)_{Al12Mg17} // (0001)_{Mg}$ and $[11\bar{1}]_{Al12Mg17} // [1\bar{2}10]_{Mg}$ as well as $(111)_{Al12Mg17} // (0001)_{Mg}$ and $[10\bar{1}]_{Al12Mg17} // [11\bar{2}0]_{Mg}$.

(5) In the thick IMCs, the microhardness in the four-phase coexistence structure dominated by Al_3Mg_2 was higher than that in the three-phase coexistence structure dominated by $Al_{12}Mg_{17}$. Furthermore, the microhardness in the upper part of the 1/2 radius zone was higher than that in the center zone in the processed coating, which resulted from the presence of the $Al_{12}Mg_{17}$ grains.

(6) The corrosion current density of the cold-sprayed Al coating was remarkably reduced, and the corrosion product was absent at the interface in different areas after FSSP, which indicated that the cold-sprayed Al coating became an effective corrosion barrier for protecting the AZ91D substrate after FSSP.

References

1. B.L. Mordike and T. Ebert, Magnesium Properties—Applications—Potential, *Mater. Sci. Eng. A*, 2001, **302**(1), p 37–45.

2. A. Luo and M.O. Pekguleryuz, Cast Magnesium Alloys for Elevated Temperature Applications, *J. Mater. Sci.*, 1994, **29**(20), p 5259–5271.

3. J. Gray and B. Luan, Protective Coatings on Magnesium and its Alloys—A Critical Review, *J. Alloys Compd.*, 2002, **336**(1–2), p 88–113.

4. H. Bu, M. Yandouzi, C. Lu and B. Jodoin, Post-Heat Treatment Effects on Cold-Sprayed Aluminum Coatings on AZ91D Magnesium Substrates, *J. Therm. Spray Technol.*, 2012, **21**(3–4), p 731–739.

5. M.X. Zhang, H. Huang, K. Spencer and Y.N. Shi, Nanomechanics of Mg-Al Intermetallic Compounds, *Surf. Coat. Technol.*, 2010, **204**(14), p 2118–2122.

6. H.Q. Sun, Y.N. Shi, M.X. Zhang and K. Lu, Surface Alloying of an Mg Alloy Subjected to Surface Mechanical Attrition Treatment, *Surf. Coat. Technol.*, 2008, **202**(16), p 3947–3953.

7. H.W. Chang, M.X. Zhang, A. Atrens and H. Huang, Nanomechanical Properties of Mg-Al Intermetallic Compounds Produced by Packed Powder Diffusion Coating (PPDC) on the Surface of AZ91E, *J. Alloys Compd.*, 2014, **587**, p 527–532.

8. C.J. Li, H.T. Wang, G.J. Yang and C.G. Bao, Characterization of High-Temperature Abrasive Wear of Cold-Sprayed FeAl Intermetallic Compound Coating, *J. Therm. Spray Technol.*, 2011, **20**(1–2), p 227–233.

9. S. Grigoriev, A. Okunkova, A. Sova, P. Bertrand and I. Smurov, Cold Spraying: From Process Fundamentals Towards Advanced Applications, *Surf. Coat. Technol.*, 2015, **268**, p 77–84. https://doi.org/10.1016/j.surfcoat.2014.09.060

10. G.J. Yang, S.N. Zhao, C.X. Li and C.J. Li, Effect of Phase Transformation Mechanism on the Microstructure of Cold-Sprayed Ni/Al-Al2o3 Composite Coatings During Post-Spray Annealing Treatment, *J. Therm. Spray Technol.*, 2013, **22**(2–3), p 398–405.

11. C.J. Li, H.T. Wang, Q. Zhang, G.J. Yang, W.Y. Li and H.L. Liao, Influence of Spray Materials and their Surface Oxidation on the Critical Velocity in Cold Spraying, *J. Therm. Spray Technol.*, 2010, **19**(1–2), p 95–101.

12. E. Irissou, J.G. Legoux, A.N. Ryabinin, B. Jodoin and C. Moreau, Review on Cold Spray Process and Technology: Part I—Intellectual Property, *J. Therm. Spray Technol.*, 2008, **17**(4), p 495–516.

13. H. Assadi, H. Kreye, F. Gärtner and T. Klassen, Cold Spraying—A Materials Perspective, *Acta Mater.*, 2016, **116**, p 382–407. https://doi.org/10.1016/j.actamat.2016.06.034

14. V. Firouzdor and S. Kou, Al-to-Mg Friction Stir Welding: Effect of Material Position, Travel Speed, and Rotation Speed, *Metall. Mater. Trans. A*, 2010, **41**(11), p 2914–2935.

15. C.G. Rhodes, M.W. Mahoney, W.H. Bingel, R.A. Spurling and C.C. Bampton, Effects of Friction Stir Welding on Microstructure of 7075 Aluminum, *Scr. Mater.*, 1997, **36**(1), p 69–75.

16. V. Firouzdor and S. Kou, Al-to-Cu Friction Stir Lap Welding, *Metall. Mater. Trans. A*, 2012, **43**(1), p 303–315.

17. S. Benavides, Y. Li, L.E. Murr, D. Brown and J.C. McClure, Low-Temperature Friction-Stir Welding of 2024 Aluminum, *Scr. Mater.*, 1999, **41**(8), p 809–815.

18. R.S. Mishra, Z.Y. Ma and I. Charit, Friction Stir Processing: A Novel Technique for Fabrication of Surface Composite, *Mater. Sci. Eng. A*, 2003, **341**(1–2), p 307–310.

19. F. Khodabakhshi, B. Marzbanrad, L.H. Shah, H. Jahed and A.P. Gerlich, Surface Modification of a Cold Gas Dynamic Spray-Deposited Titanium Coating on Aluminum Alloy by Using Friction-Stir Processing, *J. Therm. Spray Technol.*, 2019, **28**(6), p 1185–1198. https://doi.org/10.1007/s11666-019-00902-z

20. F. Khodabakhshi, B. Marzbanrad, H. Jahed and A.P. Gerlich, Interfacial Bonding Mechanisms Between Aluminum and Titanium During Cold Gas Spraying Followed by Friction-Stir Modification, *Appl. Surf. Sci.*, 2018, **462**, p 739–752. https://doi.org/10.1016/j.apsusc.2018.08.156

21. K.J. Hodder, H. Izadi, A.G. Mcdonald and A.P. Gerlich, Fabrication of Aluminium—Alumina Metal Matrix Composites via Cold Gas Dynamic Spraying at Low Pressure Followed by Friction Stir Processing, *Mater. Sci. Eng. A*, 2012, **556**, p 114–121. https://doi.org/10.1016/j.msea.2012.06.066

22. W. Li, Y. Feng, M.P. Planche, H. Liao and G. Montavon, Microstructural Evolution and Mechanical Properties Enhancement of a Cold-Sprayed Cu[Sbnd]Zn Alloy Coating with Friction Stir Processing, *Mater. Charact.*, 2017, **125**, p 76–82. https://doi.org/10.1016/j.matchar.2017.01.027

23. F. Khodabakhshi, B. Marzbanrad, A. Yazdanmehr, H. Jahed and A.P. Gerlich, Tailoring the Residual Stress During Two-Step Cold Gas Spraying and Friction-Stir Surface Integration of Titanium Coating, *Surf. Coat. Technol.*, 2019, **380**, p 125008. https://doi.org/10.1016/j.surfcoat.2019.125008

24. K. Yang, W. Li, Y. Xu and X. Yang, Using Friction Stir Processing to Augment Corrosion Resistance of Cold Sprayed AA2024/Al2o3 Composite Coatings, *J. Alloys Compd.*, 2019, **774**, p 1223–1232. https://doi.org/10.1016/j.jallcom.2018.09.386

25. T. Peat, A. Galloway, A. Toumpis, P. McNutt and N. Iqbal, The Erosion Performance of Cold Spray Deposited Metal Matrix Composite Coatings with Subsequent Friction Stir Processing, *Appl. Surf. Sci.*, 2017, **396**, p 1635–1648. https://doi.org/10.1016/j.apsusc.2016.10.156

26. F. Khodabakhshi, B. Marzbanrad, L.H. Shah, H. Jahed and A.P. Gerlich, Friction-Stir Processing of a Cold Sprayed AA7075 Coating Layer on the AZ31B Substrate: Structural Homogeneity, Microstructures and Hardness, *Surf. Coat. Technol.*, 2017, **331**, p 116–128. https://doi.org/10.1016/j.surfcoat.2017.10.060

27. Y.S. Sato, S.H.C. Park, M. Michiuchi and H. Kokawa, Constitutional Liquation During Dissimilar Friction Stir Welding of Al and Mg Alloys, *Scr. Mater.*, 2004, **50**(9), p 1233–1236.

28. Y.C. Chen and K. Nakata, Friction Stir Lap Joining Aluminum and Magnesium Alloys, *Scr. Mater.*, 2008, **58**(6), p 433–436.

29. A. Kostka, R.S. Coelho, J. dos Santos and A.R. Pyzalla, Microstructure of Friction Stir Welding of Aluminium Alloy to Magnesium Alloy, *Scr. Mater.*, 2009, **60**(11), p 953–956. https://doi.org/10.1016/j.scriptamat.2009.02.020

30. V. Firouzdor and S. Kou, Formation of Liquid and Intermetallics in Al-To-Mg Friction Stir Welding, *Metall. Mater. Trans. A*, 2010, **41**(12), p 3238–3251.

31. W. Li, C. Cao, G. Wang, F. Wang, Y. Xu and X. Yang, 'Cold Spray +' as a New Hybrid Additive Manufacturing Technology: A Literature Review, *Sci. Technol. Weld. Join.*, 2019, **24**(5), p 420–445. https://doi.org/10.1080/13621718.2019.1603851

32. W. Li, H. Assadi, F. Gaertner and S. Yin, A review of Advanced Composite and Nanostructured Coatings by Solid-State Cold Spraying Process, *Crit. Rev. Solid State Mater. Sci.*, 2019, **44**(2), p 109–156. https://doi.org/10.1080/10408436.2017.1410778

33. Z.Y. Ma, Friction Stir Processing Technology: A Review, *Metall. Mater. Trans. A*, 2008, **39**(3), p 642–658. https://doi.org/10.1007/s11661-007-9459-0

34. S. Gao, C.S. Wu, G.K. Padhy and L. Shi, Evaluation of Local Strain Distribution in Ultrasonic Enhanced Al 6061–T6 Friction Stir Weld Nugget by EBSD Analysis, *Mater. Des.*, 2016, **99**, p 135–144.

35. D. Bakavos, Y. Chen, L. Babout and P. Prangnell, Material Interactions in a Novel Pinless Tool Approach to Friction Stir Spot Welding Thin Aluminum Sheet, *Metall. Mater. Trans. A*, 2011, **42**(5), p 1266–1282.

36. W. Yuan, R.S. Mishra, B. Carlson, R. Verma and R.K. Mishra, Material Flow and Microstructural Evolution During Friction Stir Spot Welding of AZ31 Magnesium Alloy, *Mater. Sci. Eng.: A*, 2012, **543**, p 200–209. https://doi.org/10.1016/j.msea.2012.02.075

37. W. Yuan, R.S. Mishra, S. Webb, Y.L. Chen, B. Carlson, D.R. Herling and G.J. Grant, Effect of Tool Design and Process Parameters on Properties of Al Alloy 6016 Friction Stir Spot Welds, *J. Mater. Process. Technol.*, 2011, **211**(6), p 972–977. https://doi.org/10.1016/j.jmatprotec.2010.12.014

38. X. Yang, W. Feng, W. Li, Y. Xu, Q. Chu, T. Ma and W. Wang, Numerical Modelling and Experimental Investigation of Thermal and Material Flow in Probeless Friction Stir Spot Welding Process of Al 2198–T8, *Sci. Technol. Weld. Join.*, 2018, **23**(8), p 704–714. https://doi.org/10.1080/13621718.2018.1469832

39. Z. Liang, G. Qin, H. Ma, F. Yang and Z. Ao, The Constitutional Liquation at the Interface of Al/Mg Friction Welding Joints, *Sci. Technol. Weld. Join.*, 2017, **22**(5), p 363–372. https://doi.org/10.1080/13621718.2016.1248648

40. K.A. Jackson and J.D. Hunt, Lamellar and Rod Eutectic Growth, *Dyn. Curved Front.*, 1966, **2014**, p 363–376.

41. Y. Zhao, Z. Ding and Y. Chen, Crystallographic Orientations Of Intermetallic Compounds of a Multi-Pass Friction Stir Processed Al/Mg Composite Materials, *Mater. Charact.*, 2017, **128**, p 156–164. https://doi.org/10.1016/j.matchar.2017.02.005

42. M.H. Mathon, L. Allais, A.F. Gourgues and L. Naz, Texture of Welded Joints of 316L Stainless Steel, Multi-Scale Orientation Analysis of a Weld Metal Deposit, *J. Nucl. Mater.*, 2000, **277**, p 91–98.

43. A. Eghlimi, M. Shamanian, M. Eskandarian, A. Zabolian and J.A. Szpunar, Characterization of Microstructure and Texture Across Dissimilar Super Duplex/Austenitic Stainless Steel Weldment Joint by Austenitic Filler Metal, *Mater. Charact.*, 2015, **106**, p 208–217. https://doi.org/10.1016/j.matchar.2015.05.036

44. A. Hunter and M. Ferry, Phase Formation During Solidification of AISI 304 Austenitic Stainless Steel, *Scr. Mater.*, 2002, **46**(4), p 253–258.

45. Y. Liu, J. Zhou, D. Zhao and S. Tang, Investigation of the Crystallographic Orientations of the β-Mg17Al12 Precipitates in an Mg-Al-Zn-Sn Alloy, *Mater. Charact.*, 2016, **118**, p 481–485.

46. A. Panteli, J.D. Robson, I. Brough and P.B. Prangnell, The Effect Of High Strain Rate Deformation on Intermetallic Reaction During Ultrasonic Welding Aluminium to Magnesium, *Mater. Sci. Eng. A*, 2012, **556**, p 31–42. https://doi.org/10.1016/j.msea.2012.06.055

47. P. Liu, Y. Li, H. Geng and J. Wang, Microstructure Characteristics in TIG Welded Joint of Mg/Al Dissimilar Materials, *Mater. Lett.*, 2007, **61**(6), p 1288–1291.

48. D. Dietrich, D. Nickel, M. Krause, T. Lampke, M.P. Coleman and V. Randle, Formation of Intermetallic Phases in Diffusion-Welded Joints of Aluminium and Magnesium Alloys, *J. Mater. Sci.*, 2011, **46**(2), p 357–364.

49. Y.S. Sato, H. Kokawa, M. Enomoto and S. Jogan, Microstructural Evolution of 6063 Aluminum During Friction-Stir Welding, *Metall. Mater. Trans. A*, 1999, **30**(9), p 2429–2437.

50. M. Kouzeli and A. Mortensen, Size Dependent Strengthening in Particle Reinforced Aluminium, *Acta Mater.*, 2002, **50**(1), p 39–51.

51. H. Bu, M. Yandouzi, C. Lu, D. MacDonald and B. Jodoin, Cold Spray Blended Al+Mg 17Al 12 Coating for Corrosion Protection of AZ91D Magnesium Alloy, *Surf. Coat. Technol.*, 2012, **207**, p 155–162. https://doi.org/10.1016/j.surfcoat.2012.06.050

52. S. Kumar, A. Jyothirmayi, N. Wasekar and S.V. Joshi, Influence of Annealing on Mechanical and Electrochemical Properties of Cold Sprayed Niobium Coatings, *Surf. Coat. Technol.*, 2016, **296**, p 124–135. https://doi.org/10.1016/j.surfcoat.2016.04.027

53. S. Ngai, T. Ngai, F. Vogel, W. Story, G.B. Thompson and L.N. Brewer, Saltwater Corrosion Behavior of Cold Sprayed AA7075 Aluminum Alloy Coatings, *Corros. Sci.*, 2017, **2018**(130), p 231–240. https://doi.org/10.1016/j.corsci.2017.10.033

54. H. Koivuluoto, J. Lagerbom and P. Vuoristo, Microstructural Studies of Cold Sprayed Copper, Nickel, and Nickel-30% Copper Coatings, *J. Therm. Spray Technol.*, 2007, **16**(4), p 488–497.